J. Wang
School of Mechanical Engineering,
Qingdao Technological University,
Qingdao 266033, P.R.C.
e-mail: wj20011226@163.com

C. H. Venner
University of Twente,
Faculty of Engineering Technology,
Department of Engineering Fluid Dynamics,
Enschede 7500AE, The Netherlands
e-mail: C.H.Venner@utwente.nl

A. A. Lubrecht
Université de Lyon,
INSA de Lyon,
UMR CNRS 5259,
Villeurbanne F69621, France
e-mail: ton.lubrecht@insa-lyon.fr

Influence of Surface Waviness on the Thermal Elastohydrodynamic Lubrication of an Eccentric-Tappet Pair

The effect of single-sided and double-sided harmonic surface waviness on the film thickness, pressure, and temperature oscillations in an elastohydrodynamically lubricated eccentric-tappet pair has been investigated in relation to the eccentricity and the waviness wavelength. The results show that, during one working cycle, the waviness causes significant fluctuations of the oil film, pressure, and temperature, as well as a reduction in minimum film thickness. Smaller wavelength causes more dramatic variations in oil film. The fluctuations of the pressure, film thickness, temperature, and traction coefficient caused by double-sided waviness are nearly the same compared with the single-sided waviness, but the variations are less intense. [DOI: 10.1115/1.4023410]

Introduction

Machine elements, such as shafts, gears, and cam-tappet pairs, are subject to stress cycles, which eventually lead to failure due to fatigue. The cam-tappet pair is one of the important components in engines. Because of the high temperatures at friction points, scratches, tearing, early wear, etc. can easily occur; the cam-tappet pair may fail after only dozens of running hours in the worst cases. On stripping down damaged engines, the tappets were invariably found to be heavily pitted. Fatigue-related damage has significantly been alleviated, as nowadays roller-followers are used. However, for fundamental retroactive explanation of damage observed and for lessons to be learned for future roller-follower design in engines, a detailed understanding of film formation, pressure generation, and operating temperatures in lubricated contacts operating under dynamic speed entrainment conditions system is an important topic of study.

Over the years, the lubrication contacts between cam and tappet have been investigated theoretically and experimentally. In 1989, Ai and Yu [1] reported a numerical analysis for a cam-tappet pair in an internal combustion engine, presenting not only the minimum and the central film thickness but also the pressure and film distribution at some locations. Taylor [2] presented studies using a laboratory apparatus to test a direct acting mechanism and found that, in the nose region, the surface finish modification was observed, indicating a surface flattening and reduction of asperity top height. Messé and Lubrecht [3] used numerical analysis to investigate the squeeze-film effect and ejection of lubricant on hydrodynamic speed reversion of an overhead cam/tappet contact. Gangopadhyay and McWatt [4] investigated the potential to reduce friction by surface textures in a direct-acting mechanical valve train application, considering surface texture on the flat-tappet surface, and concluded that the parallel line V-grooves transverse to the entraining direction reduced the friction the most. Since the contact surfaces of the cam and the follower are usually hardened, Michalski et al. [5] studied and quantified the cam and follower wear mechanisms of a diesel direct valve-gear from the viewpoint of the material properties. Wang and Yang [6] performed a numerical analysis to simulate the thermal elastohydrodynamic lubrication (TEHL) of an eccentric-tappet pair. In order to explain the complex phenomena in a cam-follower system, Vela et al. [7,8] designed an experimental apparatus for film thickness and contact force measurement, using a purpose-built dynamic simulation program. Jang [9] simulated the EHL contact between a cam and a rolling follower pair, together with the EHL contact between a cam and a flat follower pair numerically, and showed that the rolling follower system produces a thicker film than a flat follower under the same conditions.

In the theoretical studies, in general, smooth surfaces were assumed, whereas experimental results clearly indicate an influence of surface topography on the occurrence of wear. The surface topography will lead to pressure, film, and temperature oscillations. The pressure oscillations will affect the stress cycle count that will directly lead to significant reduction of fatigue life in the solids, causing a significantly reduced service life, which may even be aggravated by a reduction of the minimum film thickness and the temperature variations. For the case of a typical cam-tappet contact, these effects have been studied in detail. The presented results contribute to the understanding of failure of cam and flat-tappet pairs.

Theoretical Model

A schematic diagram of the eccentric-tappet pair is shown in Fig. 1(*a*), where the eccentric-wheel is assumed as solid *a* and the tappet solid *b*. A dynamic coordinate system *xoz* is used in the figure, with the origin set at the nominal contact point *o*. The coordinate system is moving with the follower and the velocity components of both the eccentric-wheel and tappet face in the *z* direction equal to zero. It is well known that, in the lubrication theory, the velocity components u_a and u_b in *x*-direction refer to the relative velocities of the surfaces compared to the dynamic coordinate system. Therefore, after dynamic analyses, they are as follows:

$$\begin{cases} u_a = R\omega \\ u_b(t) = e\omega\cos\omega t \end{cases} \tag{1}$$

Thus, Fig. 1(*a*) is equivalent to Fig. 1(*b*) from an elastohydrodynamic viewpoint.

The lift of the tappet is given by

$$s(t) = e(1 - \cos\omega t) \tag{2}$$

Contributed by the Tribology Division of ASME for publication in the JOURNAL OF TRIBOLOGY. Manuscript received July 20, 2012; final manuscript received December 25, 2012; published online March 18, 2013. Assoc. Editor: Xiaolan Ai.

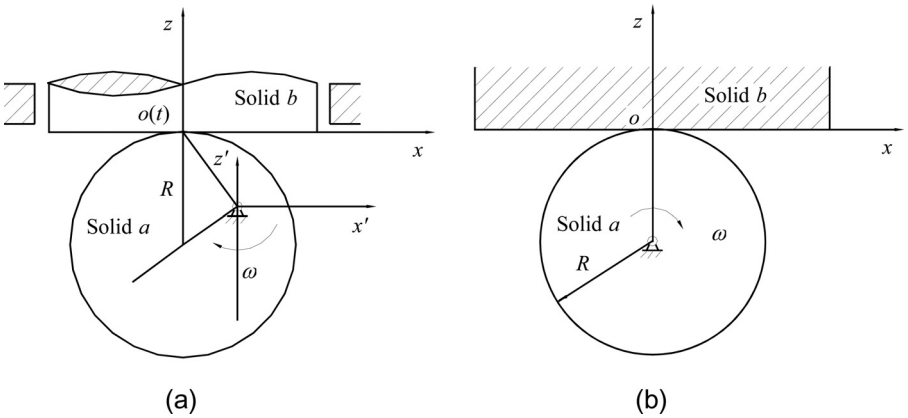

Fig. 1 Schematic diagram of an eccentric-tappet pair: (*a*) original; (*b*) equivalent

In order to facilitate the presentation of the results, the entrainment velocity is defined as

$$u_e = (u_a + u_b(t))/2 \tag{3}$$

When the solid velocities have the same magnitudes and opposite directions, a zero entraining velocity (ZEV) occurs.

Following the work of Ai and Yu [1], the load carried by the eccentric-wheel and tappet is taken to be the resultant of the inertia force F_j and the spring force F_s, with the stiffness and damping effects of the valve train neglected.

$$F(t) = F_j(t) + F_s(t) \tag{4}$$

where $F_j(t) = (m_s/3 + m_T + m_v)\ (\mathrm{d}^2 s(t)/\mathrm{d}t^2)$; $F_s(t) = F_0 + s(t) \cdot k_s$, m_s, m_T, and m_v are the masses of spring, tappet, and other correlative components; F_0 is the initial load; and k_s is the stiffness coefficient.

Supposing the width of the eccentric-wheel is L, the total load per unit length can be written as

$$w_{\mathrm{load}}(t) = \frac{F(t)}{L} = \left(F_0 + s(t) \cdot k_s + \left(\frac{1}{3}m_s + m_T + m_v\right)\frac{d^2 s(t)}{dt^2}\right)\Big/ L \tag{5}$$

where $w_0 = F_0/L$ is the initial load per unit length.

Therefore, the load equation for the contact reads

$$\int_{x_{\mathrm{in}}}^{x_{\mathrm{out}}} p(x,t)\mathrm{d}x = w_{\mathrm{load}}(t) \tag{6}$$

Yang and Wen [10] published a generalized Reynolds equation for both Newtonian and some non-Newtonian models. In this study, a Newtonian fluid flow model is assumed. For the present transient line contact problem, in the *xoz* coordinate system shown in Fig. 1(*b*), considering the possible zero entrainment velocity, this equation can be rewritten as

$$\frac{\partial}{\partial x}\left[(\rho/\eta)_{\mathrm{e}} h^3 \frac{\partial p}{\partial x}\right] = 6u_a \frac{\partial(\tilde{\rho}_a h)}{\partial x} + 6u_b \frac{\partial(\tilde{\rho}_b h)}{\partial x} + 12\frac{\partial(\rho_{\mathrm{e}} h)}{\partial t} \tag{7}$$

where $(\rho/\eta)_e$, $\tilde{\rho}_a$, and $\tilde{\rho}_b$ are equivalent quantities concerning viscosity η and density ρ of the lubricant, defined as $(\rho/\eta)_{\mathrm{e}} = 12\left(\eta_{\mathrm{e}}\rho'_{\mathrm{e}}/\eta'_{\mathrm{e}} - \rho''_{\mathrm{e}}\right)$, $\tilde{\rho}_a = 2\left(\rho_{\mathrm{e}} - \rho'_{\mathrm{e}}\eta_{\mathrm{e}}\right)$, $\tilde{\rho}_b = 2\rho'_{\mathrm{e}}\eta_{\mathrm{e}}$, $\rho_{\mathrm{e}} = (1/h)\int_0^h \rho \mathrm{d}z$, $\rho'_{\mathrm{e}} = (1/h^2)\int_0^h \rho \int_0^z 1/\eta \mathrm{d}z'\mathrm{d}z$, $\rho''_{\mathrm{e}} = (1/h^3)\int_0^h \rho \int_0^z z'/\eta \mathrm{d}z'\mathrm{d}z$, $\eta_{\mathrm{e}} = h/\int_0^h 1/\eta \mathrm{d}z$, and $\eta'_{\mathrm{e}} = h^2/\int_0^h z/\eta \mathrm{d}z$.

The solution of Eq. (7) is subject to the boundary conditions and the cavitation condition,

$$\begin{cases} p(x_{\mathrm{in}}, t) = 0, \quad p(x_{\mathrm{out}}, t) = 0 \\ p \geq 0 \quad (x_{\mathrm{in}} < x < x_{\mathrm{out}}) \end{cases} \tag{8}$$

The contact between the eccentric-tappet pair forms a finite line contact region. However, for the reason of simplification, it is treated as an infinite line contact problem. For a real contact, side leakage occurs near the edges of the contact. The effect depends on the ratio of the width of the eccentric and the contact width. If the ratio is fairly big, for example, 10, it will be quite accurate to treat the problem as a line contact. Near the edges of the contact, the sideway flows can cause side constrictions and pressure spikes and film thickness getting thinner accordingly. If the film thickness is reduced greatly, direct contact of both surfaces may occur, resulting in surface damage. Thus, the film thickness equation for a transient line contact can be written as

$$h(x,t) = h_{00}(t) + \frac{x^2}{2R} - \frac{2}{\pi E'}\int_{x_{\mathrm{in}}}^{x_{\mathrm{out}}} p(x',t)\ln(x-x')^2 \mathrm{d}x' + s_a(x,t) + s_b(x,t) \tag{9}$$

where the variable h_{00} is determined by the load Eq. (6). In Eq. (9), $s_a(x,t)$ and $s_b(x,t)$ stand for the harmonic roughness on the surfaces a and b, respectively.

$$s_a(x,t) = A_a \cos\frac{2.0[x - x_{0a}(t)]\pi}{L_a} \tag{10}$$

In Eq. (9), $x_{0\mathrm{a}}(t) = u_a t$.

$$s_b(x,t) = A_b \cos\frac{2.0[x - x_{0b}(t)]\pi}{L_b} \tag{11}$$

where $x_{0b}(t) = \int_0^t u_b(t)dt$. $x_{0\mathrm{a}}(t)$ and $x_{0b}(t)$ stand for the distances both surfaces move during time interval t from the beginning of each working cycle.

The density-pressure-temperature relation [11] is given by

$$\rho = \rho_0[1 + C_1 p/(1 + C_2 p) - D_T(T' - T'_0)] \tag{12}$$

where $C_1 = 0.6 \times 10^{-9}\,\mathrm{Pa}^{-1}$, $C_2 = 1.7 \times 10^{-9}\,\mathrm{Pa}^{-1}$, and $D_T = 0.00065\,\mathrm{K}^{-1}$.

The viscosity-pressure-temperature relation proposed by Roelands [12] is employed. It is expressed in Systeme International (SI) units as

$$\eta = \eta_0 \exp\left\{A_1\left[-1 + (1 + A_2 p)^{Z_0}(A_3 T' - A_4)^{-S_0}\right]\right\} \tag{13}$$

where $A_1 = \ln(\eta_0) + 9.67$, $A_2 = 5.1 \times 10^{-9}$, $A_3 = 1/(T'_0 - 138)$, $A_4 = 138/(T'_0 - 138)$, $S_0 = 1.1$, $Z_0 = \alpha/(A_1 A_2)$, and α is the viscosity-pressure coefficient.

The temperature field of the current problem is determined by the energy equations and their boundary conditions. In the current assumption, the body forces, the thermal radiation, and the heat conduction in x-direction are neglected. Then, for the current transient problem, the steady energy equation of the oil film used in Ref. [14] can be rewritten as

$$c\rho\left(\frac{\partial T'}{\partial t} + u\frac{\partial T'}{\partial x} - q\frac{\partial T'}{\partial z}\right) - k\frac{\partial^2 T'}{\partial z^2} = -\frac{T'}{\rho}\frac{\partial \rho}{\partial T'}\left(\frac{\partial p}{\partial t} + u\frac{\partial p}{\partial x}\right) + \eta\left(\frac{\partial u}{\partial z}\right)^2 \tag{14}$$

where $q = \frac{\partial}{\partial t}\int_0^z \rho dz + \frac{\partial}{\partial x}\int_0^z \rho u dz$. The boundary condition of Eq. (14) is $T'(x_{\text{in}}, z, t) = T'_0$ if $u(x_{\text{in}}, z, t) \geq 0$ and $T'(x_{\text{out}}, z, t) = T'_0$ if $u(x_{\text{out}}, z, t) \leq 0$.

The energy equations [14] for the two solids are

$$c_{a,b}\rho_{a,b}\left(\frac{\partial T'}{\partial t} + u_{a,b}\frac{\partial T'}{\partial x}\right) = k_{a,b}\frac{\partial^2 T'}{\partial z_{a,b}^2} \tag{15}$$

where z_a and z_b are vertical coordinates of solids a and b, respectively.

The temperature domains of solids a and b are considered to be infinite layers of finite thickness d. For solids a and b, the temperature boundary conditions in z_a and z_b directions are $T'(x, -d, t) = T'_0$ and $T'(x, d, t) = T'_0$, respectively. Other boundary conditions are: for solid a, it is given by $T'(x_{\text{in}}, z_a, t) = T'_0$; for solid b, when the solids move in the same direction, it is $T'(x_{\text{in}}, z_b, t) = T'_0$, but $T'(x_{\text{out}}, z_b, t) = T'_0$ otherwise.

On the two oil-solid interfaces, the heat flux continuity [14] conditions must be satisfied. These conditions are given by

$$k\frac{\partial T'}{\partial z}\bigg|_{z=0} = k_a\frac{\partial T'}{\partial z_a}\bigg|_{z_a=0}, \quad k\frac{\partial T'}{\partial z}\bigg|_{z=h} = k_b\frac{\partial T'}{\partial z_b}\bigg|_{z_b=0} \tag{16}$$

For Newtonian fluid, the shear stress in the oil film is expressed as

$$\tau = \tau_a + z\partial p/\partial x \tag{17}$$

By introducing $\tau = \eta(\partial u/\partial x)$ to Eq. (17) and integrating it in the z-direction, it can be obtained that

$$\tau_a = \frac{\eta_e}{h}(u_b - u_a) - h\frac{\eta_e}{\eta'_e}\frac{\partial p}{\partial x} \tag{18}$$

The traction force is calculated on surface a by

$$F'(t) = \int \tau_a(t) dx \tag{19}$$

Thus, the traction coefficient on surface a is

$$\mu(t) = \frac{F'(t)}{w_{\text{load}}(t)} = \frac{\int \tau_a(t) dx}{w_{\text{load}}(t)} \tag{20}$$

Numerical Technique

The equations are made dimensionless, introducing the following dimensionless variables (see Nomenclature):

$$P = p/p_{\text{H}}, \quad \bar{h} = hR/b^2, \quad X = x/b, \quad Z = z/h, \quad Z_{a,b} = z_{a,b}/b,$$
$$U_{a,b} = u_{a,b}/u_0, \quad U_e = u_e/u_0, \quad U_0 = \eta_0 u_0/E'R, \quad G = \alpha E',$$
$$W_0 = w_0/E'R, \quad W_{\text{load}} = w_{\text{load}}/p_{\text{H}}b, \quad \bar{T}' = T'/T'_0,$$
$$\bar{t} = tu_0/b, \quad \bar{A}_{a,b} = A_{a,b}R/b^2, \quad \bar{L}_{a,b} = L_{a,b}/b$$

Here, b is the half-width of the Hertzian contact zone under the initial load w_0, p_{H} is the maximum Hertzian pressure under w_0, and u_0 is a reference velocity introduced to facilitate the analysis. The value of u_0 has no real effect on the solution; in this paper, $U_0 = 1 \times 10^{-11}$. Selecting the film thickness h as the dimensionless reference of coordinate z can transform the irregular-shaped temperature domain into a rectangular domain, so that numerical methods can be applied easily. Another dimensionless film thickness H, defined as $H = (h/R) \times 10^5$ is used in the presentation of results.

The Reynolds, film thickness, and load equation were discretized using a uniform grid in space X and a fixed time step using a first order approximation for discretization of the wedge and squeeze term. The energy equations of the oil film and both solids are discretized also by the first order accurate scheme. At each time instant, the calculational procedure is comprised of computations of pressure and temperature repeatedly. Firstly, in the pressure iteration, the Reynolds equation, the film thickness equation, and the force balance equation are solved simultaneously by assuming the temperature field as known. Secondly, the new values of pressure and film thickness are taken into the temperature iteration as known quantities to achieve new temperature distribution. The pressure and temperature iterations are repeated until the instantaneous convergent criteria are satisfied.

$$\sum_i \left|P_i^{(\text{new})} - P_i^{(\text{old})}\right| \Big/ \sum_i P_i^{(\text{new})} < 1 \times 10^{-4} \tag{21}$$

$$\left|\Delta X \sum_i P_i^{(\text{new})} - W_{\text{load}}\right| \Big/ W_{\text{load}} < 1 \times 10^{-4} \tag{22}$$

$$\sum_i \sum_j \left|\bar{T}_{i,j}^{(\text{new})} - \bar{T}_{i,j}^{(\text{old})}\right| \Big/ \sum_i \sum_j \bar{T}_{i,j}^{(\text{new})} < 1 \times 10^{-5} \tag{23}$$

where superscripts "old" and "new" represent the status before and after an iteration at one moment. The relative errors of pressure, load, and temperature are associated with Eqs. (21), (22), and (23), respectively. The reader can go to Ref. [6] for more details of the pressure and temperature iterations.

The simultaneous system of the Reynolds, film thickness, and load equations are solved using a multigrid (MG) technique. It essentially follows the work of Venner and Lubrecht [13], with modifications to account for the variations of viscosity and density across the film. The numerical results were obtained using a domain $-4.5 \leq X \leq 4.5$ and a grid with 961 points in X direction and six levels in the MG algorithm.

The temperature computation is carried out on the finest grid level with 21 equidistance nodes in Z direction across the film and 12 nonequidistant nodes in Z_a and Z_b directions within solids a and b, respectively. In one working cycle, from $T = 0.25$ to 0.75, the two surfaces move in opposite directions; consequently, the slide-roll ratio exceeds 2. The technique proposed by Yang et al. [14] is applied to such places successfully. One working cycle was subdivided into 11,520 time steps. The accuracy was investigated by comparing results with smaller time steps and mesh sizes, from which it was concluded that the resulting solutions have an estimated accuracy of a few percent.

The procedures were repeated for a number of working/loading cycles until the solution was settled in the periodic behavior associated with the waviness characteristics considered. The periodic convergent criteria are

$$\sum_i \left|P_i^{(\text{now})} - P_i^{(\text{pre})}\right| \Big/ \sum_i P_i^{(\text{now})} < 1 \times 10^{-3} \tag{24}$$

$$\left|\Delta X \sum_i P_i^{(\text{now})} - \Delta X \sum_i P_i^{(\text{pre})}\right| \Big/ \Delta X \sum_i P_i^{(\text{now})} < 1 \times 10^{-3} \tag{25}$$

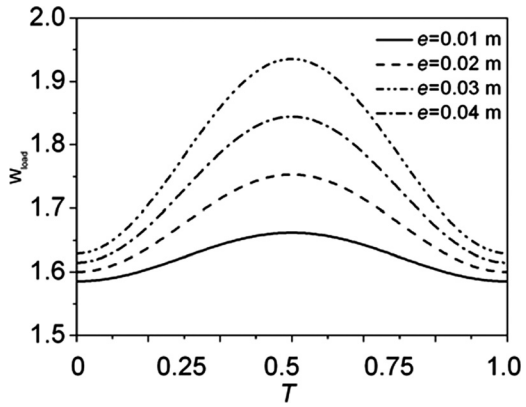

Fig. 2 Variations of dimensionless load with eccentricities over a working cycle

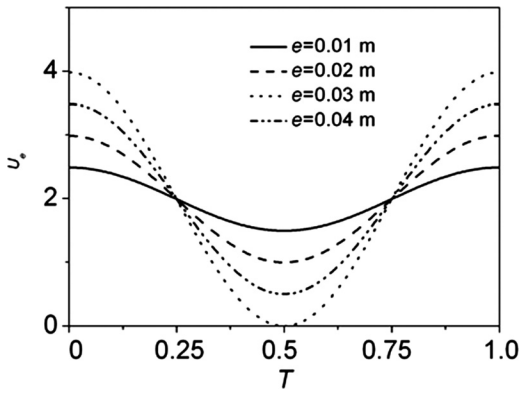

Fig. 3 Variations of dimensionless entrainment velocity with eccentricity over a working cycle

$$\sum_i \sum_j \left| \bar{T}_{i,j}^{(\text{now})} - \bar{T}_{i,j}^{(\text{pre})} \right| \Big/ \sum_i \sum_j \bar{T}_{i,j}^{(\text{now})} < 1 \times 10^{-4} \qquad (26)$$

where superscripts "pre" and "now" represent the $T = 0.5$ time instant in the previous and present working cycles, when the load is maximum and the slide-roll ratio is the biggest. The calculation is finished when the criteria are reached.

Results

Operating Conditions. In this section, TEHL results for a steel-steel line contact problem are presented by using the following parameters: for the lubricant, $\eta_0 = 0.08$ Pa s, $\alpha = 2.2 \times 10^{-8}$ m^2/N, $\rho_0 = 875$ kg/m^3, $c = 2000$ J/kg K, and $k = 0.14$ W/m K; for the two solids, $\rho_{a,b} = 7850$ kg/m^3, $c_{a,b} = 470$ J/kg K, and $k_{a,b} = 46$ W/m K. Other common input data include: $G = 5000$, $d = 3.15$, $T'_0 = 313$ K, $R = 0.04$ m, $W = 0.8 \times 10^{-4}$ ($p_H = 0.811$ GPa), $U_0 = 1 \times 10^{-11}$, $m_s = 0.2$ kg, $m_T = 0.4$ kg, $m_v = 0.595$ kg, $L = 0.02$ m, $k_s = 49$ N/mm, and angular speed of the eccentric-wheel shaft $\omega = 36\pi$ rad/s. The eccentricities of the eccentric-wheel are 0.01 m, 0.02 m, 0.03 m, and 0.04 m, respectively.

Figure 2 depicts the variation of the dimensionless load parameter with the above four eccentricities over a working cycle. In Fig. 2, $W_{\text{load}} = w_{\text{load}}(t)/p_H b$, from Eq. (2) and (5), it can be understood that the load increases with the eccentricity for the same time instant and gets to its summit at $T = 0.5$.

Figure 3 presents the variation of the dimensionless entraining velocity with the above four eccentricities over a working cycle. The velocity of solid a keeps constant, while that of solid b changes with the eccentricity and time. At $T = 0.5$, from Eq. (1), the velocity of solid b gets to its bottom.

Single-Sided Waviness. Figure 4 shows the variation of the central oil pressure with the four eccentricities during one working

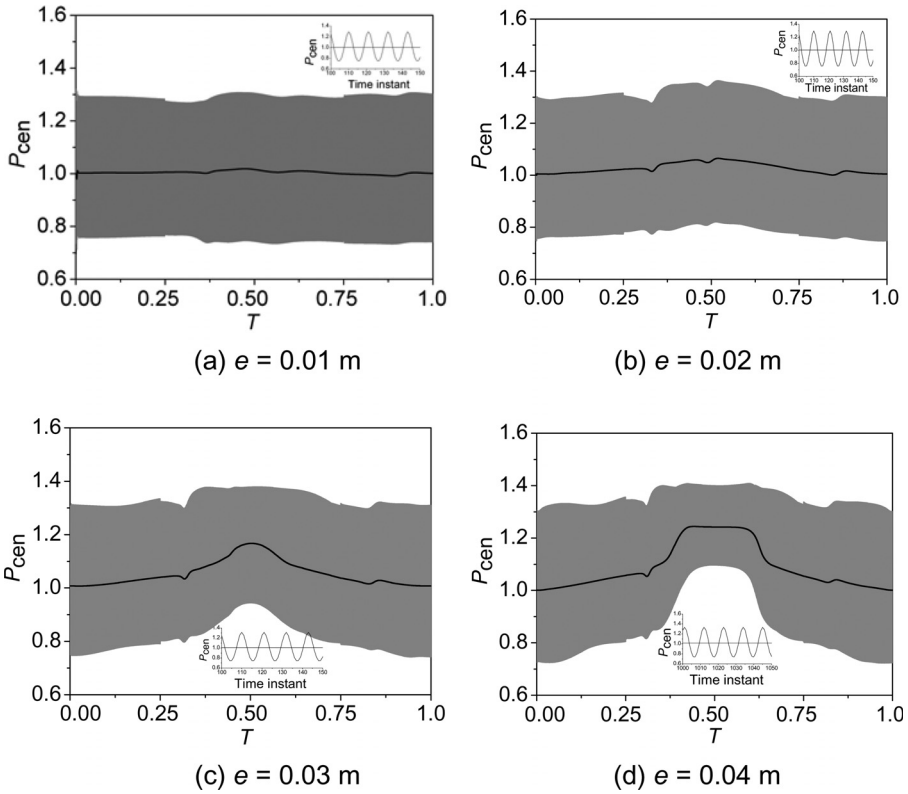

Fig. 4 Variation of the central pressure over one period, $A_b = 0.2\ \mu$m, $L_b = 240\ \mu$m

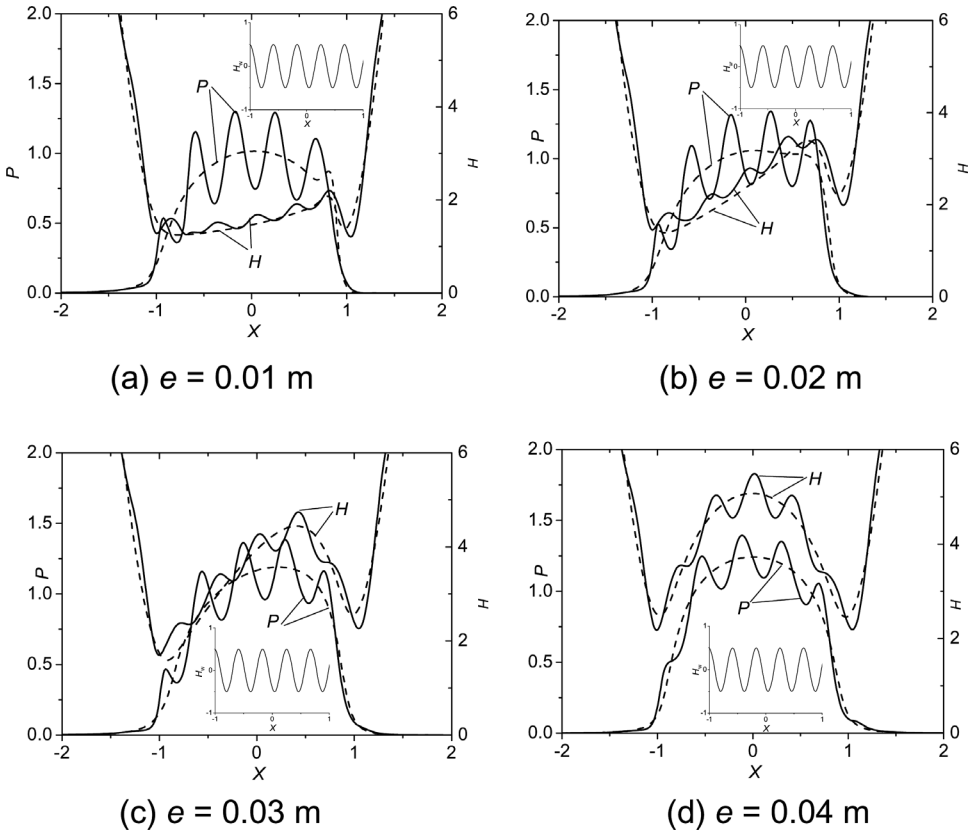

Fig. 5 Pressure and film thickness profiles at $T = 0.5$, $A_b = 0.2\,\mu$m, $L_b = 240\,\mu$m

cycle, $A_b = 0.2\,\mu$m and $L_b = 240\,\mu$m. The surface waviness causes dramatic fluctuations, shown in the figures as the gray amplitude zone. The small drawing situated inside of each figure presents the variation of the central pressure during a short time interval (50 time instants). The solid black line in each gray amplitude zone is the periodical central pressure of the smooth contact. For the same time instants from $T = 0.25$ to 0.75, the slide-roll ratio increases with the increase in the eccentricity. During this half working period, the variation of the oil film in the contact is controlled by the "temperature-viscosity wedge effect" [14], which is enhanced by the increase in eccentricity and consequently results in a significant temperature rise and pressure increase. Figure 4 shows that the smooth central pressure provides a reference against which the rough central pressure fluctuates. In Figs. 4(*a*) and 4(*b*), the fluctuation amplitude is roughly in a range of $0.75 \sim 1.3$. In Figs. 4(*c*) and 4(*d*), when the two surfaces move in the same direction, the fluctuation amplitude is also roughly in the same range. But during $T = 0.25 \sim 0.75$, with the increase of the eccentricity, smooth central pressure profile achieves a plateau and an elevated value significantly above the maximum Hertzian pressure; consequently, the rough central pressure profile uplifts it shape correspondingly. However, the fluctuation amplitude of the central pressure is reduced.

In order to explain the reduction in the gray zone amplitude, Fig. 5 shows the pressure and film thickness profiles at $T = 0.5$ with the four eccentricities. In the figures, the smooth pressure and film thickness profiles are also presented for comparison. In each figure, the corresponding undeformed waviness in dimensionless form is shown as a reference. It is seen from Fig. 5(*a*) that the amplitude deformation of the waviness was greatly influenced by the pressure. As a result, the waviness deforms elastically and most of the waviness is suppressed by the pressure. With the increase of the eccentricity, the "temperature-viscosity wedge effect" [14] is enhanced, producing higher pressure and temperature. Higher temperature lowers the viscosity within the oil film and results in smaller pressure fluctuation. In Fig. 4(*d*), the slide-roll ratio turns to infinite (ZEV condition); the elastic deformation of the waviness is small.

Figure 6 gives the temperature rise curves at midlayer of the oil and on both surfaces at $T = 0.5$ for the four eccentricities. As the eccentricity increases, the midlayer oil temperature increases for both smooth and wavy surfaces. Figure 6 shows that, with the increase in eccentricity, the surface waviness causes fluctuations in the midlayer oil temperature. However, the fluctuation amplitude of the temperature rise at the midlayer of oil film decreases. Moreover, the temperature rise on both surfaces becomes smaller and tends to be symmetrical with the $X = 0$ line.

Corresponding isothermal calculations were also carried out. The fluctuation amplitudes of the gray zones for central pressure are wider than those in Fig. 4, and in the half period with opposite motion, the amplitudes are larger than those when the two surfaces move in the same direction. As for the isothermal pressure and film thickness profiles at $T = 0.5$ with the four eccentricities, the film thickness decreases, and the reduction in the waviness amplitude increases with the increase in the eccentricity. Therefore, it is clarified that the thermal effect plays an important role in the elastic deformation of the waviness.

Figures 7–9 present the variations of the minimum film thickness, the maximum temperature rise, and traction coefficient over one working cycle with the four eccentricities. Figure 7 shows that the minimum film thickness fluctuates with the smooth minimum film thickness asymmetrically, proving that, for different time instants and eccentricities, the deformation of the waviness is different. Generally, the waviness reduces the minimum film thickness periodically. Figure 8 shows that the waviness causes a temperature rise of roughly 30–40 °C. In Figs. 9(*a*)–9(*c*), the surface waviness reduces the traction coefficient due to the temperature rise. In Fig. 9(*d*), at $T = 0$, the two surfaces share the same velocity. Then the velocity of surface b begins to increase. From $T = 0.75$, the velocity of surface b is zero and thereafter increases

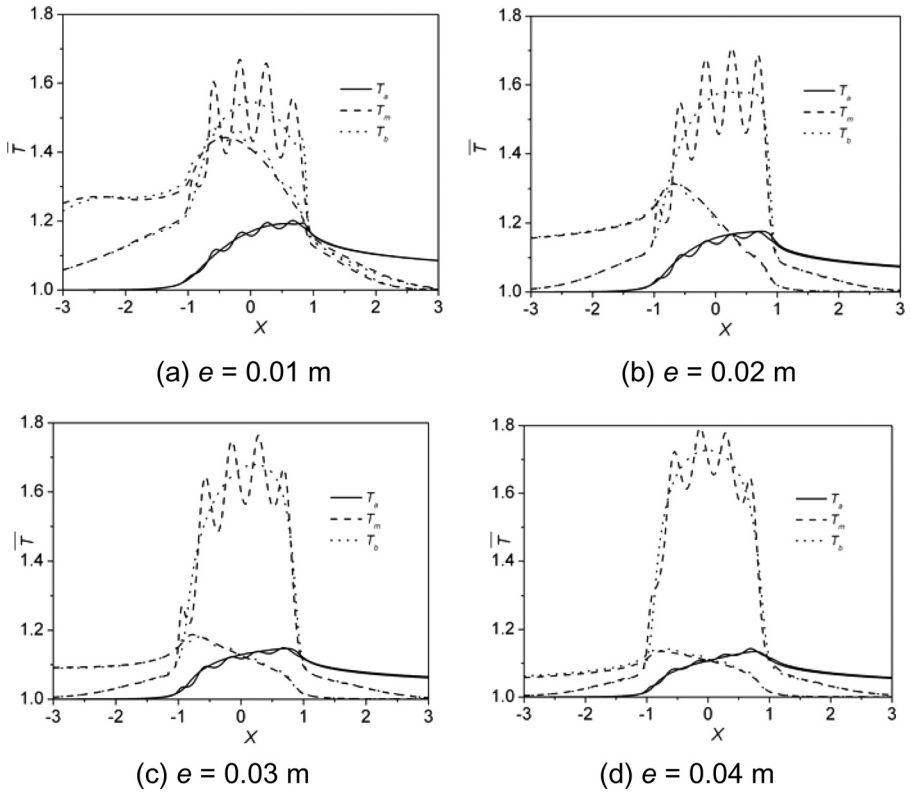

Fig. 6 Temperature rise profiles at $T = 0.5$, $A_b = 0.2\ \mu$m, $L_b = 240\ \mu$m

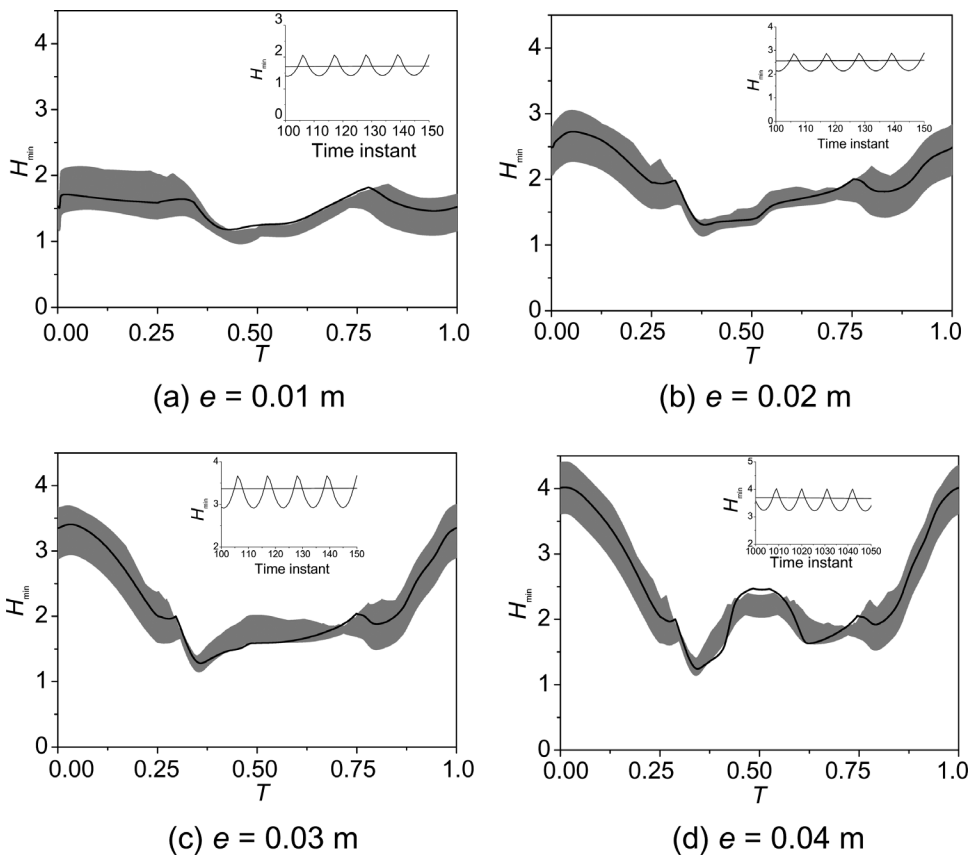

Fig. 7 Variation of the minimum film thickness over one period, $A_b = 0.2\ \mu$m, $L_b = 240\ \mu$m

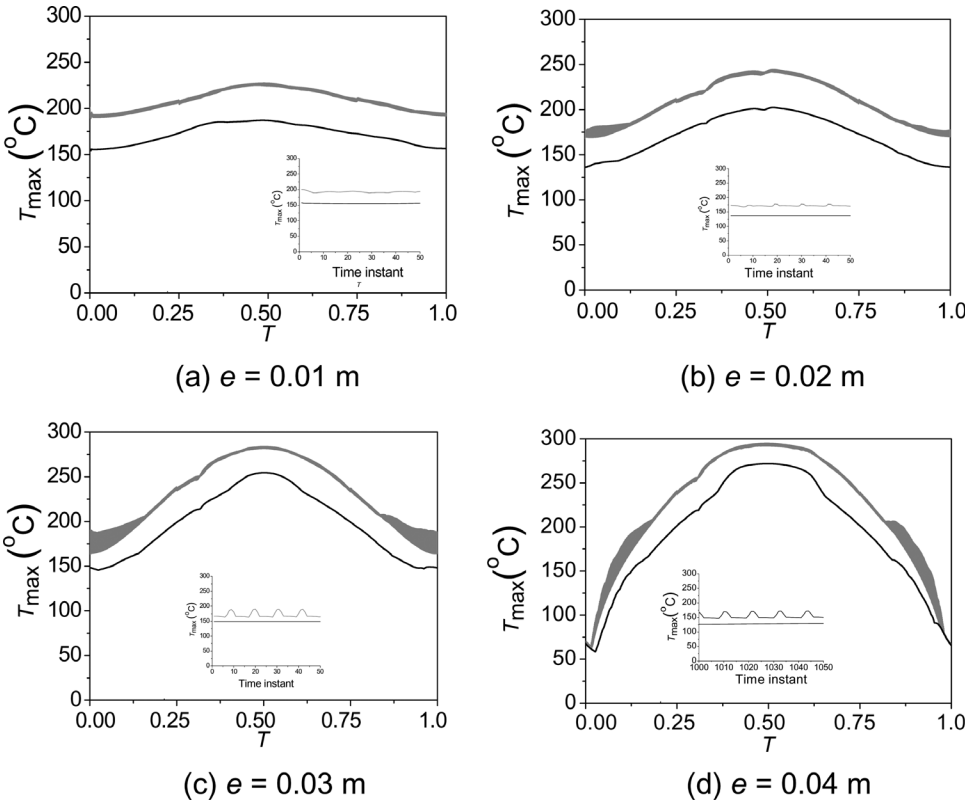

Fig. 8 Variation of the maximum temperature over one period, $A_b = 0.2\,\mu$m, $L_b = 240\,\mu$m

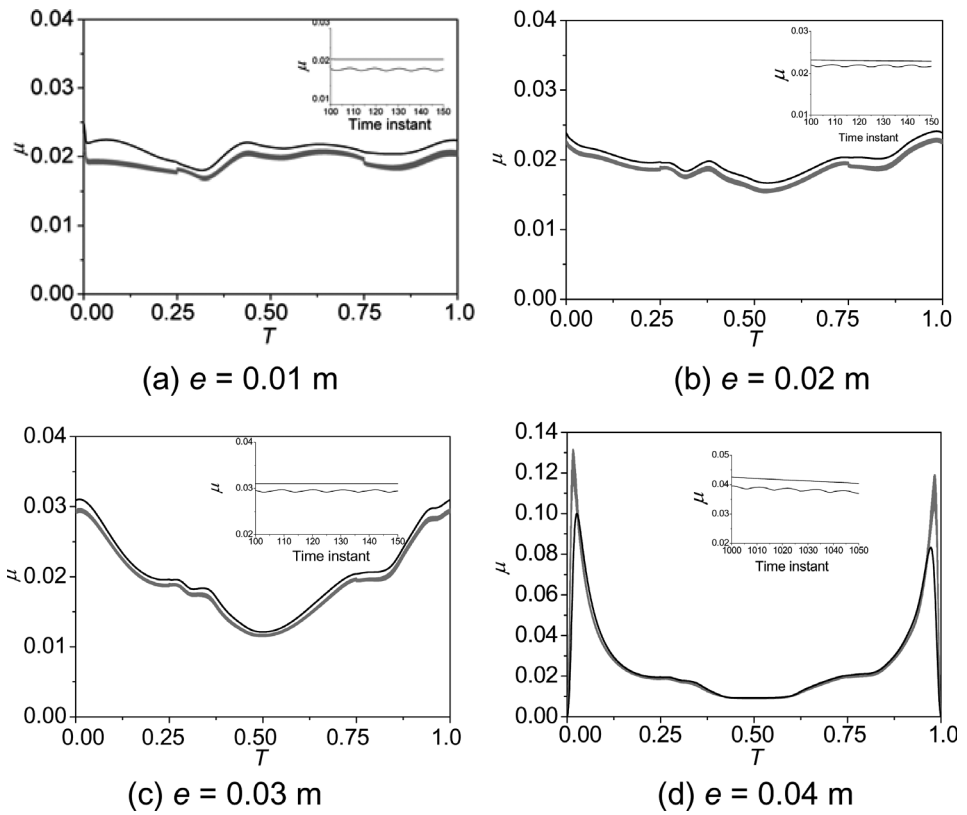

Fig. 9 Variation of the traction coefficient over one period, $A_b = 0.2\,\mu$m, $L_b = 240\,\mu$m

up to the velocity of surface a at $T = 1.0$. The variation of the velocity of surface b in Fig. 8(*d*) results in the two peaks in the smooth traction coefficient. With the consideration of the surface waviness, the quick change in the shear stress causes an increase in the height of the two peaks. Apart from the two peaks, the rough traction coefficient is smaller than the smooth one.

Figure 10 shows the variation of the central pressure for $e = 0.01$ m, and the wavelength of the harmonic waviness is

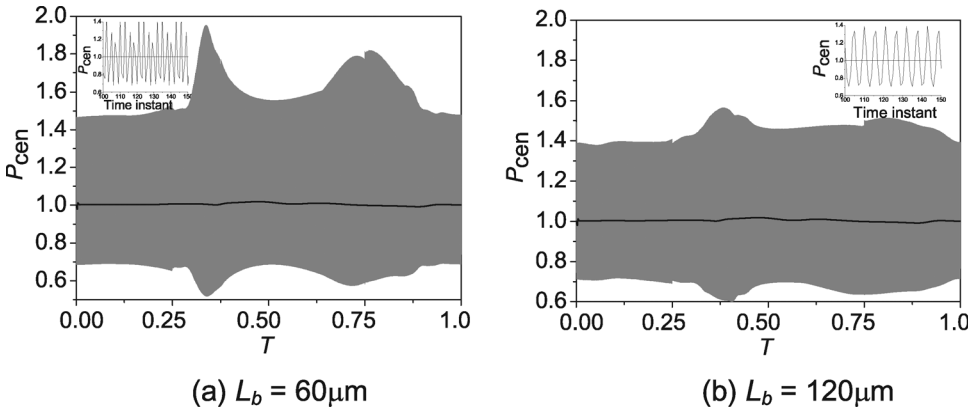

Fig. 10 Variation of the central pressure versus roughness wavelength

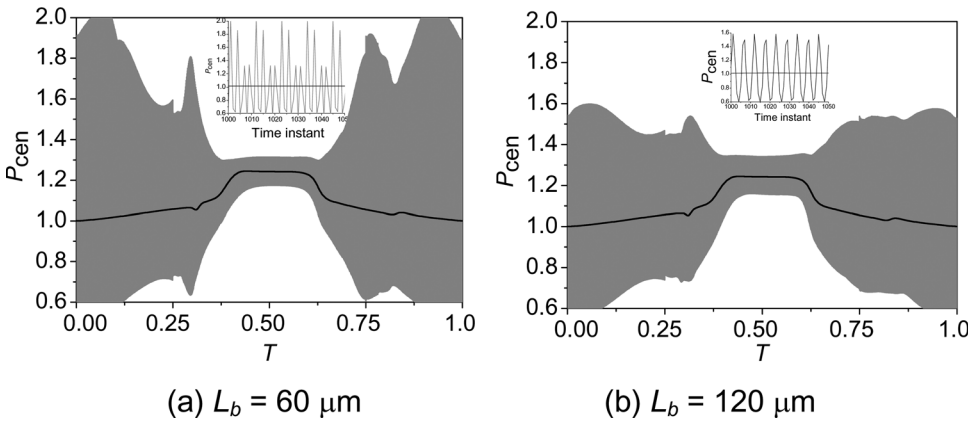

Fig. 11 Variation of the central pressure versus roughness wavelength, $A_b = 0.2\,\mu$m, $e = 0.04$ m

60 μm and 120 μm, respectively. Compared with Fig. 4(*a*), the amplitude of the central pressure is wider and obviously more detrimental. In Fig. 10(*b*), the central pressure fluctuation is still larger than that in Fig 4(*a*).

Figure 11 shows the variation of the central pressure for $e = 0.04$ m, and the wavelength is 60 μm and 120 μm, respectively. Compared with Figs. 4(*d*) and 11(*a*), it is seen that, for a smaller wavelength (Fig. 11(*a*)), the fluctuation of the central pressure during the same-direction half period is dramatic. However, during the opposite-direction half period, the pressure fluctuation is reduced significantly. The current results show that a smaller wavelength is more detrimental to the contact. Wang et al. [15] pointed out in their steady state point contact thermal EHL analyses that there exists an extreme value when the wavelength turns from 0 to infinite. This extreme value produces a maximum pressure fluctuation. In machining work or surface treatment, such an extreme value should be avoided overall anyway.

Double-Sided Waviness. Calculations for the four eccentricities with double-sided surface waviness, $A_a = A_b = 0.1\,\mu$m ($A_a + A_b = 0.2\,\mu$m) were also carried out. Figure 12 shows the variations of the central pressure for the four eccentricities with double-sided surface waviness, $A_a = A_b = 0.1\,\mu$m and $L_a = L_b = 240\,\mu$m. The fluctuation amplitudes of the central pressure under the four eccentricities are all roughly the same as those in Fig. 4. However, the overlap and offset of both surfaces' waviness makes the distribution of central pressure vary less intense as those in Fig. 4. So do the minimum film thickness and the traction coefficient. The only big difference exists only in the considerable variation of the periodical maximum temperature, shown in Fig. 13.

Figure 14 shows the variation of central pressure over one period, $A_a = A_b = 0.1\,\mu$m and $L_a = L_b = 120\,\mu$m for $e = 0.01$ m and 0.04 m, respectively. Compared with Figs. 10(*a*) and 11(*b*), the fluctuation of the central pressure is less intense. But the fluctuation is larger at some localities, for example, around $T = 0.4$ for Fig. 14(*a*) and $T = 0.3$ and 0.75 for Fig. 14(*b*).

Discussion

The film thickness ratio λ has been a valuable design concept, since it has led to an appreciation of the occurrence of surface interaction in a range of lubricated machine elements and a recognition that surface topography can have a highly significant role in the performance and durability of such components. This is certainly true in regard to the cam-tappet pair addressed in this paper. λ is defined as the ratio of the film thickness (calculated through the application of classical thin film analysis taking the surfaces to be smooth) to the composite surface roughness. Values of the film thickness ratio appropriate to what are now called regimes of lubrication have frequently been quoted and employed as design criteria. However, the position is complicated by many factors, including the recognition that roughness measured in the laboratory may be modified during operation and/or flattened during a particular load event [2]. The Amplitude Reduction Theory (ART) [16,17] predicts the deformation as a function of a single parameter ∇ in pure rolling and rolling-sliding conditions, containing the wavelength and the operating conditions. The deformation of real roughness was studied using optical interferometric technique by Sperka et al. [18]. The attenuation of the waviness in Fig. 5 involved the thermal effect. In order to understand the

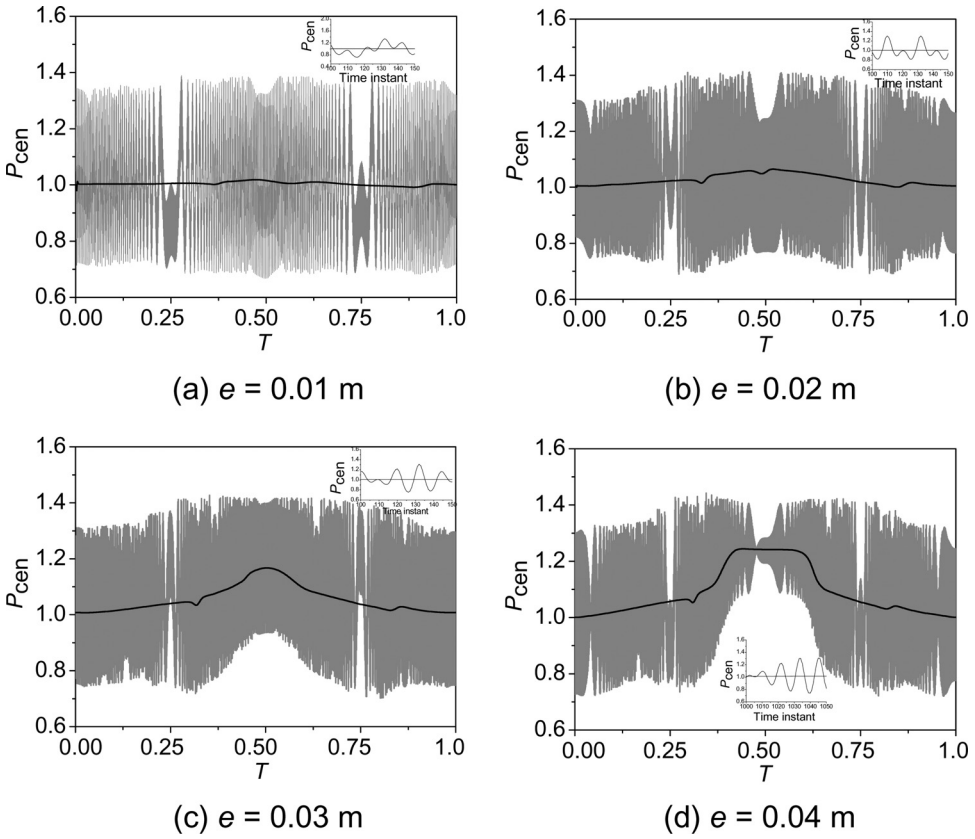

Fig. 12 Variation of the central pressure over one period with double-sided waviness, $A_a = A_b = 0.1\ \mu$m, $L_a = L_b = 240\ \mu$m

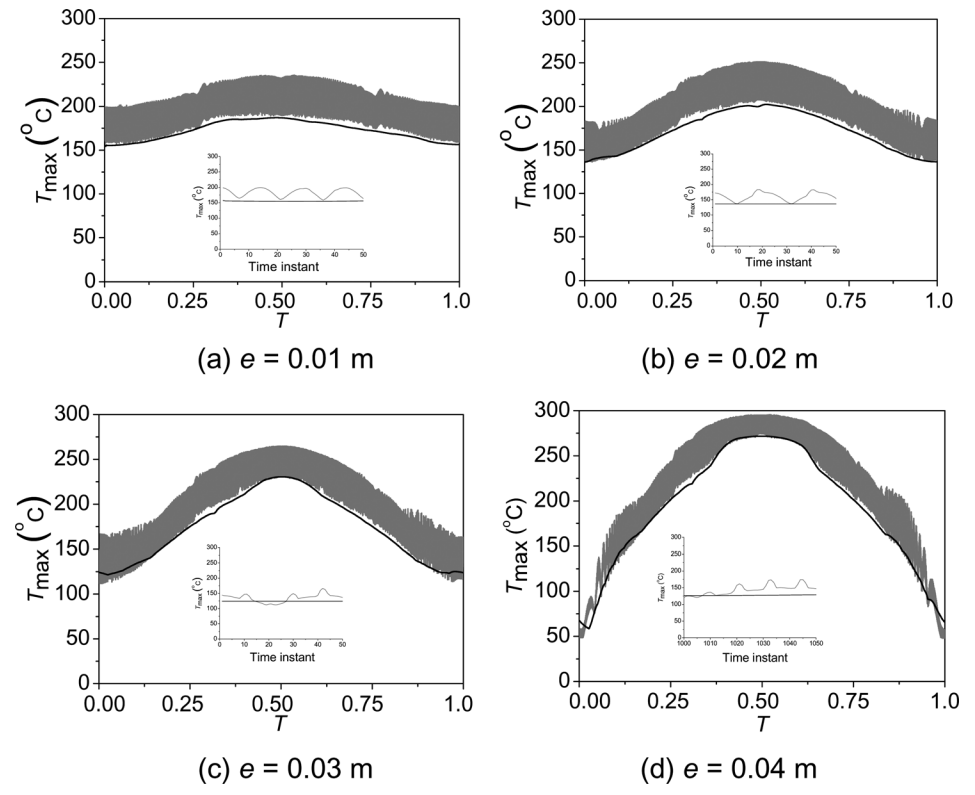

Fig. 13 Variation of the maximum temperature over one period with double-sided waviness, $A_a = A_b = 0.1\ \mu$m, $L_a = L_b = 240\ \mu$m

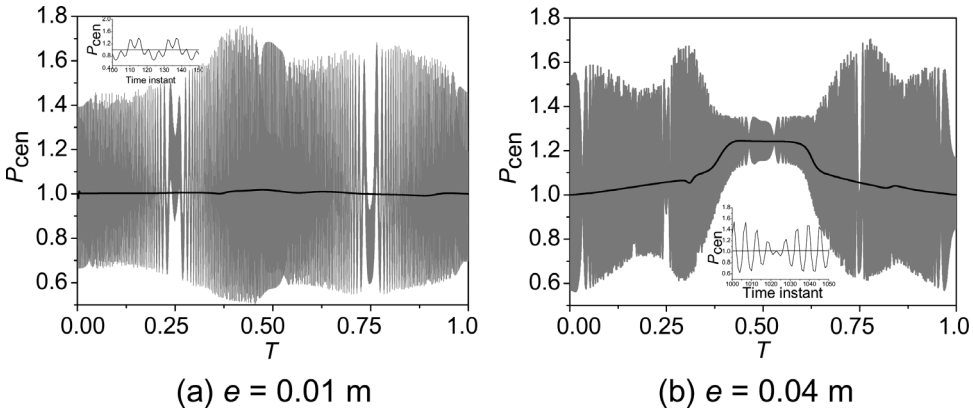

Fig. 14 Variation of the central pressure over one period with double-sided waviness, $A_a = A_b = 0.1\ \mu$m, $L_a = L_b = 120\ \mu$m

thermal effect on the amplitude reduction, more research needs to be carried out.

Conclusions

(1) Considering the harmonic waviness on the surface of the flat-tappet pair, strong and intense fluctuation of oil film pressure, film thickness, temperature rise, and traction coefficient are created during one working cycle. With the decrease in the wavelength, the fluctuation of the pressure becomes more dramatic. It also changes the distribution of the film thickness, oil temperature, and traction coefficient significantly.

(2) During the half period when the two solids move oppositely, for the same wavelength, with the increase of the eccentricity, the deformation of the surface waviness becomes smaller. The variation of the oil film is also controlled by the "temperature-viscosity wedge" effect.

(3) For the contact with double-sided waviness, the fluctuation of the pressure, film thickness, temperature, and traction coefficient are nearly the same compared with the single-sided waviness, but the variations are less intense.

Acknowledgment

This work is supported by the National Natural Science Foundation of China for supporting this work through grants 51075221 and 51275253. The authors would like to thank Professor Peiran Yang of Qingdao Technological University for valuable discussion.

Nomenclature

$A_{a,b}$ = amplitude of waviness on surfaces a and b
b = half-width of Hertzian contact zone at load w_0, m
c, c_a, c_b = specific heat of lubricant and solids, J/kg K
d = thickness of thermal layers in solids, m
$\bar{d}$ = dimensionless thickness of thermal layers in solids
e = eccentricity of eccentric-wheel, m
E' = effective Young's modulus, Pa
H = dimensionless film thickness for results, $(h/R) \times 10^5$
h = film thickness, m
h_{00} = rigid central film thickness, m
$\bar{h}$ = dimensionless film thickness for calculation, hR/b^2
k, k_a, k_b = thermal conductivity of lubricant and solids, W/m K
L = length of the eccentric-wheel, m
L_a, L_b = wavelength of the waviness on surfaces a and b
p = hydrodynamic pressure, Pa
p_H = maximum Hertzian pressure at load w_0, Pa
R = radius of the eccentric-wheel, m
R_a = composite surface roughness, m
s = lift of the flat tappet, m
t = time, s
T = dimensionless period
T' = temperature, K
T'_0 = ambient temperature, K
$\bar{T}$ = dimensionless temperature, T'/T'_0
$\bar{T}_{max}$ = dimensionless maximum temperature
u = x-component of lubricant velocity, m/s
u_0 = reference velocity, m/s
$u_{a,b}$ = velocities of solids a, b, m/s
u_e = entraining velocity, m/s
U_0 = dimensionless reference velocity
w = z-component of lubricant velocity, m/s
w_{load} = applied load per unit length, N/m
x = horizontal coordinate, m
x_{in}, x_{out} = start and end of film, m
z, z_a, z_b = vertical coordinates of film and solids, m
α = Barus' viscosity-pressure coefficient, m^2/N
η = viscosity of lubricant, Pa s
η_0 = ambient viscosity of lubricant, Pa s
ω = angular speed of the eccentric-wheel
Σ = transient slide-roll ratio, $2(u_a - u_b)/(u_a + u_b)$
ρ, ρ_a, ρ_b = densities of lubricant and solids, kg/m^3
ρ_0 = ambient density of lubricant, kg/m^3
λ = film thickness ratio, h/R_a

References

[1] Ai, X., and Yu, H., 1989, "A Numerical Analysis for the Transient EHL Process of a Cam-Tappet Pair in I.C. Engine," ASME J. Tribol., **111**, pp. 413–417.
[2] Taylor, C. M., 1998, "Automobile Engine Tribology—Design Considerations for Efficiency and Durability," Wear, **221**, pp. 1–8.
[3] Messé, S., and Lubrecht, A. A., 2000, "Transient Elastohydrodynamic Analysis of an Overhead Cam/Tappet Contact," Proc. Inst. Mech. Eng., Part J: J. Eng. Tribol., **214**, pp. 415–425.
[4] Gangopadhyay, A., and McWatt, D. G., 2008, "The Effect of Novel Surface Textures on Tappet Shims on Valvetrain Friction and Wear," Tribol. Trans., **51**(2), pp. 221–230.
[5] Michalski, J., Marszalek, J., and Kubiak, K., 2000, "An Experimental Study of Diesel Engine Cam and Follower Wear With Particular Reference to the Properties of the Materials," Wear, **240**, pp. 168–179.
[6] Wang, J., and Yang, P., 2003, "A Numerical Analysis for TEHL of Eccentric-Tappet Pair Subjected to Transient Load," ASME J. Tribol., **125**, pp. 770–779.
[7] Vela, D., Fazzolari, F., and Ciulli, E., 2011, "Dynamic Aspects of a New Experimental Apparatus for Tribological Investigations on Cam-Follower Pairs," 13th World Congress in Mechanism and Machine Science, Guanajuato, Mexico, 19–25 June, Paper No. A19-504.
[8] Vela, D., Cuilli, E., Piccigallo, B., and Fazzolari, F., 2011, "Investigation on Cam-Follower Lubricated Contacts," Proc. Inst. Mech. Eng., Part J: J. Eng. Tribol., **225**, pp. 379–392.
[9] Jang, S., 2008, "Transient Elastohydrodynamic Lubrication Film Thickness in Sliding and Rolling Line Contacts," J. Mech. Sci. Technol., **22**, pp. 946–956.
[10] Yang, P., and Wen, S., 1990, "A Generalized Reynolds Equation for Non-Newtonian Thermal Elastohydrodynamic Lubrication," ASME J. Tribol., **112**, pp. 631–636.

[11] Zhu, D., and Wen, S., 1984, "A Full Numerical Solution for the Thermoelastohydrodynamic Problem in Elliptical Contact," ASME J. Tribol., **106**, pp. 246–254.
[12] Roelands, C. J. A., 1966, "Correlation Aspects of Viscosity-Temperature-Pressure Relationship of Lubricating Oils," Ph.D. thesis, Delft University of Technology, The Netherlands.
[13] Venner, C. H., and Lubrecht, A. A., 2000, *Multilevel Methods in Lubrication*, Elsevier, New York.
[14] Yang, P., Qu, S., Chang, Q., and Guo, F., 2001, "On the Theory of Thermal Elastohydrodynamic Lubrication at High Slide-Roll Ratios: Line Contact Solution," ASME J. Tribol., **123**, pp. 36–41.
[15] Wang, J., Kaneta, M., Guo, F., and Yang, P., 2006, "Occurrence of Micro-EHL in Simple Sliding Motion With Transverse Roughness," Proc. Inst. Mech. Eng., Part J: J. Eng. Tribol., **220**, pp. 273–285.
[16] Hooke, C. J., and Venner, C. H., 2000, "Surface Roughness Attenuation in Line and Point Contacts," Proc. Inst. Mech. Eng., Part J: J. Eng. Tribol., **214**, pp. 439–444.
[17] Wang, J., Venner, C. H., and Lubrecht, A. A., 2011, "Amplitude Reduction in EHL Line Contacts Under Rolling Sliding Conditions," Tribol. Int., **44**(12), pp. 1997–2001.
[18] Sperka, P., Krupka, I., and Hartl, M., 2010, "Experimental Study of Real Roughness Attenuation in Concentrated Contacts," Tribol. Int., **43**, pp. 1893–1901.